

Balanced cross-Kerr coupling for superconducting qubit readout

Alex A. Chapple,^{1,*} Othmane Benhayoune-Khadraoui,^{1,*} Simon Richer,¹ and Alexandre Blais^{1,2}

¹*Institut Quantique and Département de Physique,
Université de Sherbrooke, Sherbrooke J1K 2R1 Quebec, Canada*

²*CIFAR, Toronto, ON M5G 1M1, Canada*

(Dated: January 16, 2025)

Dispersive readout, the standard method for measuring superconducting qubits, is limited by multiphoton qubit-resonator processes arising even at moderate drive powers. These processes degrade performance, causing dispersive readout to lag behind single- and two-qubit gates in both speed and fidelity. In this work, we propose a novel readout method, termed “*junction readout*”. Junction readout leverages the nonperturbative cross-Kerr interaction resulting from coupling a qubit and a resonator via a Josephson junction. Furthermore, by adding a capacitive coupling in parallel to the junction, Purcell decay can be suppressed without the need for a Purcell filter. We also show that junction readout is more robust against deleterious multiphoton processes, and offers greater flexibility for resonator frequency allocation. Crucially, junction readout achieves superior performance compared to dispersive readout while maintaining similar hardware overhead. Numerical simulations show that junction readout can achieve fidelities exceeding 99.99% in under 30 ns, making it a promising alternative for superconducting qubit readout with current hardware.

Introduction.— Fast and high-fidelity qubit measurement is a cornerstone of quantum information processing and fault-tolerant quantum computing. For example, in quantum error correction (QEC) protocols, each round of QEC relies on rapid single-shot readout of ancilla qubits to detect errors. Recent breakthroughs achieving break-even performance in surface [1, 2] and bosonic codes [3–5] have relied on dispersive readout, a standard tool for measuring superconducting qubits. This readout operates by introducing a qubit-state dependent shift in the resonator frequency, enabling qubit state inference without directly disturbing the qubit [6–8].

Despite the improvements in readout fidelity and integration times [9–13], dispersive readout still lags behind the performance of the best single- and two-qubit gates. Increasing the readout drive power to enhance fidelity and speed often leads to measurement-induced transitions [14–21] which are detrimental to error correction protocols as they introduce correlated errors [22, 23]. Resetting such states, which typically involve ~ 5 to 10 photons [19], is challenging even with the use of leakage reduction techniques [24–27]. Thus, achieving fast, high-fidelity readout with low leakage rates remains an open problem.

To further complicate matters, state-of-the-art dispersive readout often requires a Purcell filter to prevent the qubit from decaying through the readout channel [28, 29]. While effective, adding a Purcell filter increases the readout system’s footprint, complicates calibration, and makes multiplexing more challenging. These challenges have spurred interest in intrinsically Purcell-protected qubits and readout methods as compact, scalable alternatives for next-generation quantum processors [30–34].

Here, we propose an approach to mediate a nonperturbative dispersive qubit-resonator interaction, enabling

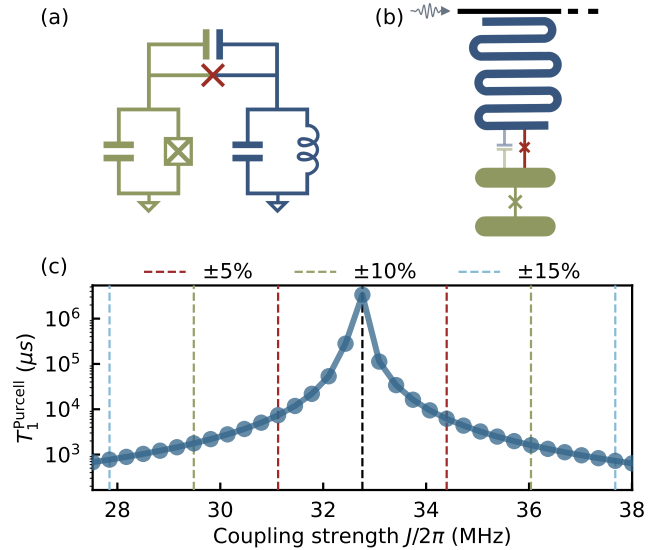


FIG. 1. (a) Transmon (green) coupled to a readout resonator (blue) via a Josephson junction (red) and a capacitor. (b) Possible experimental realization of the junction readout circuit with feedline (black). (c) Purcell-limited lifetime T_1^{Purcell} of the transmon for varying capacitive coupling strengths J . The black dashed line indicates where the cancellation condition of Eq. (3) is met. There, $J/2\pi \simeq 32.8$ MHz, corresponding to a coupling capacitance of 10 fF.

high-fidelity and fast measurement without the need for a Purcell filter. Even when accounting for reduced readout efficiency and finite qubit lifetime, our approach achieves an order-of-magnitude improvement over state-of-the-art readout systems with comparable hardware overhead.

Theory of junction readout.— In circuit QED, the dispersive interaction $\sum_{i_t} \chi_{i_t} |i_t\rangle \langle i_t| \hat{a}^\dagger \hat{a}$, with $|i_t\rangle$ a bare transmon state and \hat{a} the resonator’s annihilation operator, is usually realized by capacitively coupling a qubit

* These authors contributed equally.

and a resonator that are widely detuned in frequency [8]. Here, we seek an alternative circuit that mediates this interaction, with the interaction strength $2\chi_z = \chi_{1_t} - \chi_{0_t}$ engineered to be nonperturbative (i.e., independent of the qubit-resonator detuning and not obtained after some Schrieffer-Wolff-type frame transformation).

Alternative strategies for engineering a nonperturbative Kerr interaction have been explored [31–36]. In contrast to these approaches, which often involve complex circuit designs, rely on special symmetries, or encode qubits in spatially delocalized modes, our proposed circuit, shown in Fig. 1, offers a simpler solution with hardware overhead comparable to that of dispersive readout. In this circuit, the transmon (green) is coupled to a readout resonator (blue) through a Josephson junction in parallel with a capacitor whose role will be discussed below. The Hamiltonian of this circuit takes the form

$$\begin{aligned} \hat{H} &= 4E_c(\hat{n}_t - n_g)^2 - E_J \cos \hat{\varphi}_t + \omega_r \hat{a}^\dagger \hat{a} \\ &\quad - E_{J_c} \cos(\hat{\varphi}_t - \hat{\varphi}_r) + J \hat{n}_t \hat{n}_r \\ &\equiv \hat{H}_{\text{tr}} + \hat{H}_r + \hat{H}_{\text{int}}, \end{aligned} \quad (1)$$

where $\hat{\varphi}_t$ and \hat{n}_t are the transmon's phase and charge operators, and E_J and E_c are its Josephson and charging energies, respectively. The resonator has frequency ω_r , and its phase operator is given by $\hat{\varphi}_r = \varphi_{\text{zpf}r}(\hat{a} + \hat{a}^\dagger)$ where $\varphi_{\text{zpf}r} = (2\pi/\Phi_0)\sqrt{\hbar Z_r/2}$ is the phase zero-point fluctuations. Furthermore, E_{J_c} is the Josephson energy of the coupling junction, and J is the capacitive coupling strength between the transmon and the resonator. The gate charge n_g is included explicitly, as it has been shown to affect the onset of measurement-induced transitions [18, 19, 21, 37]. As we show below, our proposed circuit ensures a high measurement critical photon number regardless of the value of the gate charge.

Setting $J = 0$ for the moment, the coupling Hamiltonian can be written in the form

$$\hat{H}_{\text{int}} = -E_{J_c} \cos \hat{\varphi}_t \cos \hat{\varphi}_r - E_{J_c} \sin \hat{\varphi}_t \sin \hat{\varphi}_r. \quad (2)$$

To second order in phase fluctuations, the cos-cos interaction of the first term leads to $\hat{\varphi}_t^2 \hat{\varphi}_r^2$, thereby mediating a nonperturbative cross-Kerr coupling. As discussed in Ref. [38], this results in large measurement critical photon numbers and no Purcell decay. When supplemented with the appropriate resonator drive [38], this interaction emulates the longitudinal coupling discussed in Ref. [32], enabling fast and accurate discrimination of the pointer states. Here, we show that the circuit of Fig. 1 achieves the aforementioned benefits with a significantly simplified design. On the other hand, to first order in phase fluctuations, the sin-sin interaction term is an unwanted Jaynes-Cummings interaction that causes multiphoton resonances [15–19], thereby lowering the critical photon number, see Sec. S3 A of [39]. A potential mitigation strategy involves increasing the detuning between the qubit and resonator while increasing the qubit-resonator coupling to maintain a constant dispersive shift [40, 41]. However, this requires the use of

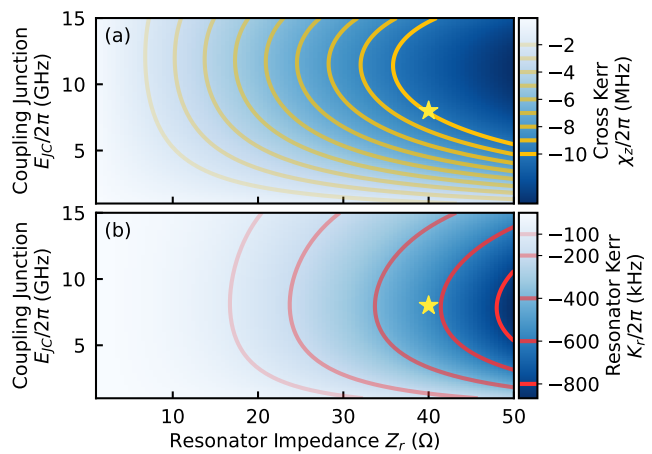


FIG. 2. (a) Cross-Kerr coupling χ_z and (b) resonator self-Kerr K_r between the transmon and the resonator for varying resonator impedance Z_r and coupling junction energy E_{J_c} . The contour lines indicate lines of constant (a) cross-Kerr ranging from -2 to -10 MHz and (b) self-Kerr ranging from -100 to -800 kHz. The star marks the parameter used in the readout simulations of Fig. 4.

low-frequency qubits strongly coupled to high-frequency resonators which poses its own set of challenges. Additionally, for moderate detunings, this approach leads to Purcell-limited qubit lifetimes, necessitating the use of a Purcell filter.

Instead, here we propose to cancel this unwanted sin-sin term by introducing a parallel capacitance to the Josephson junction which mediates a charge-charge coupling $J\hat{n}_t\hat{n}_r$, see Fig. 1. The coupling strength J is specifically chosen to cancel the Purcell decay by setting the $0 \leftrightarrow 1$ matrix element of the interaction Hamiltonian to zero, as expressed by the condition

$$\begin{aligned} -E_{J_c} \langle 1_t, 0_r | \sin \hat{\varphi}_t \sin \hat{\varphi}_r | 0_t, 1_r \rangle \\ + J \langle 1_t, 0_r | \hat{n}_r \hat{n}_t | 0_t, 1_r \rangle = 0, \end{aligned} \quad (3)$$

where $|j_r\rangle$ denotes a bare resonator state. Intuitively, this condition describes destructive interference between the current paths through the capacitor and the junction, flowing from the qubit to the readout feedline. Importantly, since the cancellation condition involves only the computational subspace, the optimal coupling strength J is insensitive to fluctuations in the gate charge n_g . Moreover, as shown in Fig. 1(c), the residual Purcell decay remains minimal even when the condition Eq. (3) is not perfectly satisfied. For instance, with a $\sim 10\%$ imperfection in the junction or capacitor fabrication, the Purcell decay time T_1 remains on the order of ~ 1 ms for the chosen parameters [39], highlighting the robustness of this scheme to fabrication errors.

Choice of readout parameters.— We now turn to a discussion of the optimal choice of parameters. To achieve fast readout we aim for a large transmon-resonator cross-Kerr interaction. However, as is evident

from Eq. (2), a nonperturbative cross-Kerr term (resulting from $\hat{\varphi}_i^2 \hat{\varphi}_r^2$) is inherently accompanied by a nonperturbative self-Kerr nonlinearity on the resonator (resulting from $\hat{\varphi}_r^4$). A large self-Kerr can bananize the coherent state in the resonator [42, 43], potentially reducing readout fidelity by hindering the clear separation of pointer states and limiting the maximum photon population in the resonator. Moreover, this distortion renders the conventional linear measurement filter suboptimal for state assignment [44–46].

To achieve a large cross-Kerr interaction without compromising the linearity of the readout resonator, we optimize the resonator impedance Z_r . From Eq. (2), the leading contribution of the cross-Kerr strength is given by $\chi_z \simeq -\varphi_{\text{zpf}}^2 E_{Jc} \sqrt{2E_C/E_{J,\text{total}}}/2$, with $E_{J,\text{total}} = E_J + E_{Jc}$ which we keep constant. The self-Kerr nonlinearity of the resonator inherited from the coupling junction is approximately $K_r \simeq -E_{Jc} \varphi_{\text{zpf}}^4/4$. As a result, the cross-Kerr interaction decreases quadratically with the resonator phase zero-point fluctuations φ_{zpf} , while the self-Kerr decreases quartically with φ_{zpf} . Conversely, both χ_z and K_r increase linearly with respect to the coupling junction energy E_{Jc} . Since φ_{zpf} depends on the resonator impedance Z_r , we optimize Z_r and E_{Jc} to achieve a large cross-Kerr coupling with minimal self-Kerr nonlinearity. Fig. 2(a) and (b) show the cross-Kerr coupling strength χ_z and the resonator’s self-Kerr K_r extracted from exact numerical diagonalization of Eq. (1) for a range of resonator impedances Z_r and coupling strengths E_{Jc} . For realistic circuit parameters, we are able to achieve a cross-Kerr coupling comparable to standard dispersive readout, typically ranging from 2 to 10 MHz. Furthermore, by slightly reducing the resonator impedance below the conventional 50Ω —something that is easily achievable experimentally—the self-Kerr nonlinearity can be tuned to match, or in some cases even fall below, the typical values of 100 to 500 kHz observed in standard dispersive readout.

Interestingly, we also observe that, in junction readout, the dispersive shift shows minimal variation with increasing resonator photon numbers, in contrast to dispersive readout, where the dispersive shift decreases significantly. This difference arises from the nature of the qubit-resonator interaction which is different in the two schemes. Indeed, in junction readout, the cos-cos interaction leads to smaller higher-order corrections to the dispersive shift at large photon numbers compared to dispersive readout, enabling a faster readout as the cross-Kerr coupling remains large even when the resonator is populated, see [39] for further details.

The above analysis reveals that junction readout produces qubit-state-dependent frequency shifts similar to those of dispersive readout, suggesting comparable performance at first glance. In the following, we highlight the significant advantages offered by junction readout, demonstrating its superiority over dispersive readout in key aspects, namely its larger robustness against measurement-induced transitions, as well as faster and

higher fidelity measurements.

Suppressing ionization.— The quantum nondemolition (QND) nature of dispersive readout is challenged by multiphoton processes arising due to accidental degeneracies between the qubit and the resonator [15]. This phenomenon, also referred to as ionization, occurs when two states of the transmon-resonator system become resonant as photons populate the resonator, leading to a sudden population transfer from the resonator to the transmon [15–19, 21, 47]. Because this process can typically involve highly-excited states of the transmon which are charge sensitive, the resonator critical photon number n_{crit} at which these multiphoton processes occur can fluctuate widely with gate charge [18, 19, 37, 48]. We now show junction readout is far more robust against such multiphoton processes than dispersive readout.

To assess this robustness, we compute the critical photon numbers using branch analysis, a numerical tool predicting the onset of ionization and that has been shown to match experimental observations [48]; see Ref. [39] for further details in the context of junction readout. Fig. 3 shows, given an arbitrary gate charge in the range $[0, 0.5]$, the percentage of instances where the critical photon number exceeds $n_{\text{crit}} = 35$ for both junction readout (blue) and dispersive readout (red), across a wide resonator frequency range of $\omega_r/2\pi \sim 6 - 10$ GHz. To ensure a fair comparison between both approaches, the dispersive shift is fixed to $\chi_z/2\pi \simeq 9$ MHz across all values of ω_r . For the dispersive readout, this requires adjusting the qubit-resonator coupling at all values of the resonator frequency [8]. The value of n_{crit} reported in Fig. 3 is arbitrary but chosen to correspond to a readout fidelity of approximately 99.99%, given the dispersive shift used here, see Sec. S3 B of [39]. We first observe that for junction readout there exists a wide ~ 3 GHz range of resonator frequencies for which junction readout reaches near 100% certainty of achieving a critical photon number exceeding 35 photons. In contrast, for dispersive readout there exists no frequency range for which the critical photon number consistently exceeds this threshold. Furthermore, dispersive readout has less flexibility for frequency allocation as the dispersive shift depends on the detuning, and often requires the readout resonator to be close in frequency to the qubit for a large dispersive shift. On the other hand, junction readout relies on a nonperturbative cross-Kerr interaction which does not depend on the detuning, and thus offers greater flexibility for frequency allocation and potentially can alleviate frequency crowding issues for large-scale chips, whilst maintaining a large cross-Kerr for fast readout.

Another important consequence of the cancellation condition of Eq. (3) is to push ionization to larger photon numbers. Indeed, from perturbation theory, when the transmon ionizes to an excited state outside of the computational manifold, the transition occurs through virtual excitations, sequentially climbing the intermediate states between the initial state and the final ionized state [48]. The cancellation condition in Eq. (3), how-

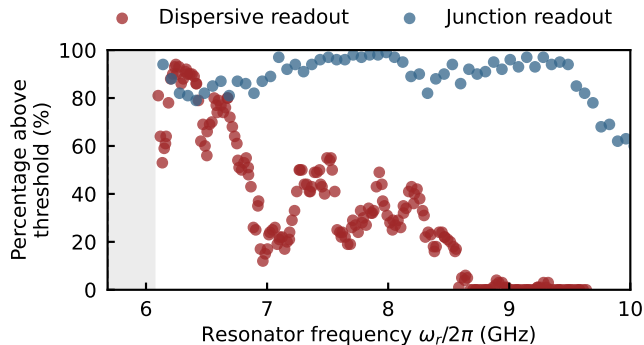


FIG. 3. Percentage of instances where the critical photon number exceeds $n_{\text{crit}} = 35$ with varying gate charge on the transmon for both junction readout (blue) and dispersive readout (red). In both cases, the dispersive shift is set to a constant value of $\chi_z/2\pi \simeq 9$ MHz. With a qubit frequency of $\omega_q/2\pi \simeq 5.68$ GHz, the shaded region corresponds to resonator frequencies that are outside of the dispersive regime.

ever, eliminates the matrix element responsible for the transition between the ground state and the first excited state, thereby preventing the initial step of leaving the computational subspace from the ground state. Additionally, while not exact, this cancellation approximately suppresses the matrix element responsible for transitions from the first to the second excited state, further reducing ionization when the qubit begins in its first excited state.

Readout performance.— We have shown that junction readout can realize a large cross-Kerr together with manageable resonator self-Kerr, as well as higher critical photon numbers compared to dispersive readout across a large resonator frequency range, all without the need for Purcell filters. We now present numerical simulations of junction readout suggesting that fast, high-fidelity, and quantum nondemolition readout of transmons can be achieved with realistic parameters.

Our simulations are based on integrating the stochastic Schrödinger equation for heterodyne measurements of the resonator first assuming an ideal readout efficiency $\eta = 1$ [49], see [39] for further details. Because they use the full Hamiltonian Eq. (1), these simulations account for the cross-Kerr, $\chi_z/2\pi \simeq 10$ MHz, but also the deleterious effect of the resonator self-Kerr, $K_r/2\pi \simeq 489$ kHz. A two-step measurement pulse leading to an average photon number of $\bar{n} \simeq 40$ photons is used, well below the critical photon number of $n_{\text{crit}} = 65$. Despite this short integration time, we find a large separation of the measurement result distribution for the two initial state using an optimal discriminator (black dashed line), see Fig. 4(b). The resulting assignment error vs the integration time (full dark blue line) is reported in panel (c). For $\eta = 1$, a measurement fidelity of 99.99% is obtained in as short as $t_m = 20$ ns. Furthermore, we find a QNDness of 99.89% and 99.71% for the ground and excited state, respectively [39].

Because of the small resonator self-Kerr, the distortion of the qubit-state-dependent resonator coherent states is relatively small, see Fig. 4(a). Under this condition, the resonator state can be approximated as coherent, allowing us to compare our numerical results with the analytical expression for the signal-to-noise ratio (SNR) and the assignment error [8, 39, 50]. The assignment error derived from this approximation (full light blue line) closely matches the full stochastic simulations. The small discrepancy is primarily due to the self-Kerr nonlinearity of the resonator. Given the good agreement between the numerical simulation and the coherent-state approximation, we use the latter to estimate the readout fidelity for finite transmon lifetime and nonideal readout efficiency, something which would be otherwise numerically challenging. First, for $T_1 = 30 \mu\text{s}$ (red triangles), the readout fidelity comfortably exceeds 99.9% in $t_m \simeq 17$ ns. For a longer-lived transmon with $T_1 = 120 \mu\text{s}$ (green squares), the fidelity surpasses 99.99% at $t_m \simeq 21$ ns. Secondly, assuming an infinite T_1 but a readout efficiency of $\eta = 0.5$ consistent with state-of-the-art experiments [10, 13, 20], we find a similar readout performance (dashed light blue line). Additionally, using quantum optimal control, we can further decrease the assignment error, reaching a readout fidelity of 99.99% in $t_m \simeq 18$ ns with realistic pulse shapes [39]. We emphasize that these results are based on parameters readily achievable with current hardware. Even accounting for reduced efficiencies and T_1 limitations, our results indicate that junction readout could achieve a fidelity exceeding 99.99% in under 30 ns, outperforming state-of-the-art readout experiments by an order of magnitude.

Conclusion.— We have presented a circuit mediating a nonperturbative cross-Kerr coupling between a qubit and a readout resonator. The proposed junction readout method outperforms state-of-the-art dispersive readout by achieving higher critical photon numbers across a broad range of resonator frequencies and is less susceptible to the effect of gate charge. Notably, junction readout does not require Purcell filters and has comparable hardware overhead to dispersive readout. Even when accounting for finite qubit lifetimes and reduced readout efficiencies, this approach achieves a readout fidelity of 99.99% in under 30 ns. Junction readout overcomes many of the limitations posed by dispersive readout and can be implemented readily with only small modifications to current hardware. Junction readout could become a standard method for superconducting qubit measurement in next-generation quantum processors.

Note.— During the preparation of this manuscript, we learned of similar work experimentally demonstrating Josephson junction-based readout of a transmon qubit. [51]. In contrast to our approach, in that work the resonator nonlinearity induced by the coupling junction is large such that a high-power bifurcation readout is used.

Acknowledgments.— The authors are grateful to Cristóbal Lledó for a critical reading of the manuscript.

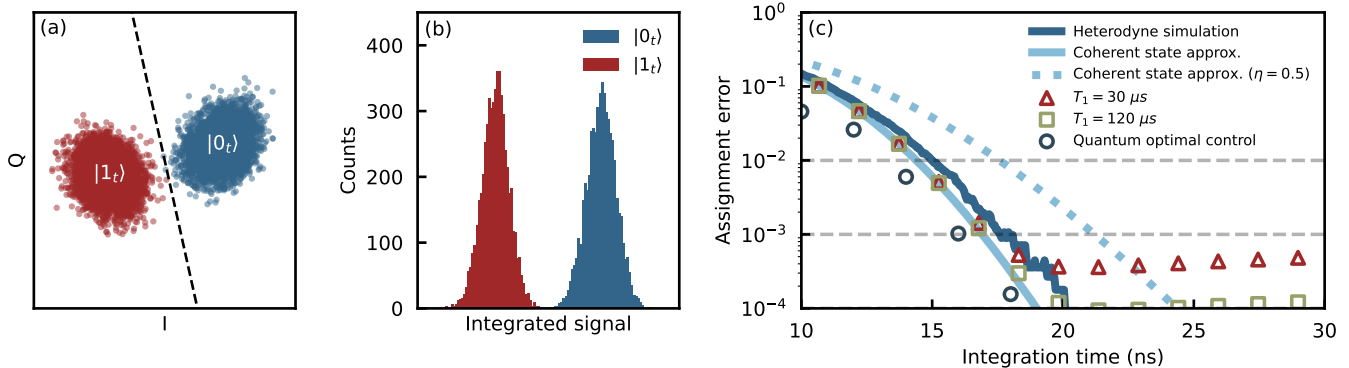


FIG. 4. (a) IQ-plane of 11,200 single-shot heterodyne readout simulations of a transmon with junction readout. The black dashed line is the optimal discriminator of the two blobs corresponding to the qubit prepared in the ground (blue) or excited state (red). (b) Histogram of the integrated signal using an optimal discriminator. For both (a) and (b) the integrated time is $t_m \simeq 20$ ns. (c) Assignment error obtained from the stochastic heterodyne readout simulations compared to coherent state approximated assignment error. Using the coherent state approximated assignment error, we also show the assignment error for readout efficiency of $\eta = 0.5$ (where $0 \leq \eta \leq 1$) as well as when T_1 is 30 or 120 μs . Moreover, we show that quantum optimal control (QOC) further improves the readout fidelity. Here, the transmon charging energy is $E_C/2\pi = 300$ MHz with $E_{J,\text{total}}/E_C = 50$ and gate charge $n_g = 0.0$. The resonator frequency is $\omega_r/2\pi = 9.375$ GHz, with resonator impedance $Z_r = 40\Omega$. The junction coupling strength is $E_{J_c}/2\pi = 8$ GHz. This set of parameter results in a cross-Kerr of $\chi_z/2\pi \simeq 10$ MHz, and a critical photon number of $n_{\text{crit}} = 65$.

This work was undertaken thanks in part to funding from the U.S. Army Research Office Grant No. W911NF-23-1-

0101. Additional support is acknowledged from NSERC, the Canada First Research Excellence Fund, and the Ministère de l'Économie et de l'Innovation du Québec.

-
- [1] G. Q. AI, Suppressing quantum errors by scaling a surface code logical qubit, *Nature* **614**, 676 (2023).
- [2] G. Q. AI and Collaborators, Quantum error correction below the surface code threshold, *Nature* [10.1038/s41586-024-08449-y](https://doi.org/10.1038/s41586-024-08449-y) (2024).
- [3] N. Ofek, A. Petrenko, R. Heeres, *et al.*, Extending the lifetime of a quantum bit with error correction in superconducting circuits, *Nature* **536**, 441 (2016).
- [4] V. V. Sivak, A. Eickbusch, B. Royer, *et al.*, Real-time quantum error correction beyond break-even, *Nature* **616**, 50 (2023).
- [5] B. L. Brock, S. Singh, A. Eickbusch, V. V. Sivak, A. Z. Ding, L. Frunzio, S. M. Girvin, and M. H. Devoret, *Quantum error correction of qubits beyond break-even* (2024), [arXiv:2409.15065 \[quant-ph\]](https://arxiv.org/abs/2409.15065).
- [6] A. Blais, R.-S. Huang, A. Wallraff, S. M. Girvin, and R. J. Schoelkopf, Cavity quantum electrodynamics for superconducting electrical circuits: An architecture for quantum computation, *Phys. Rev. A* **69**, 062320 (2004).
- [7] A. Wallraff, D. I. Schuster, A. Blais, L. Frunzio, J. Majer, M. H. Devoret, S. M. Girvin, and R. J. Schoelkopf, Approaching unit visibility for control of a superconducting qubit with dispersive readout, *Phys. Rev. Lett.* **95**, 060501 (2005).
- [8] A. Blais, A. L. Grimsmo, S. M. Girvin, and A. Wallraff, Circuit quantum electrodynamics, *Rev. Mod. Phys.* **93**, 025005 (2021).
- [9] D. T. McClure, H. Paik, L. S. Bishop, M. Steffen, J. M. Chow, and J. M. Gambetta, Rapid driven reset of a qubit readout resonator, *Phys. Rev. Appl.* **5**, 011001 (2016).
- [10] T. Walter, P. Kurpiers, S. Gasparinetti, P. Magnard, A. Potočnik, Y. Salathé, M. Pechal, M. Mondal, M. Oppliger, C. Eichler, and A. Wallraff, Rapid high-fidelity single-shot dispersive readout of superconducting qubits, *Phys. Rev. Appl.* **7**, 054020 (2017).
- [11] Y. Sunada, S. Kono, J. Ilves, S. Tamate, T. Sugiyama, Y. Tabuchi, and Y. Nakamura, Fast readout and reset of a superconducting qubit coupled to a resonator with an intrinsic purcell filter, *Phys. Rev. Appl.* **17**, 044016 (2022).
- [12] F. Swiadek, R. Shillito, P. Magnard, A. Remm, C. Hellings, N. Lacroix, Q. Ficheux, D. C. Zanuz, G. J. Norris, A. Blais, S. Krinner, and A. Wallraff, Enhancing dispersive readout of superconducting qubits through dynamic control of the dispersive shift: Experiment and theory (2023), [arXiv:2307.07765 \[quant-ph\]](https://arxiv.org/abs/2307.07765).
- [13] P. A. Spring, L. Milanovic, Y. Sunada, S. Wang, A. F. van Loo, S. Tamate, and Y. Nakamura, *Fast multiplexed superconducting qubit readout with intrinsic purcell filtering* (2024), [arXiv:2409.04967 \[quant-ph\]](https://arxiv.org/abs/2409.04967).
- [14] J. E. Johnson, C. Macklin, D. H. Slichter, R. Vijay, E. B. Weingarten, J. Clarke, and I. Siddiqi, Heralded state preparation in a superconducting qubit, *Phys. Rev. Lett.* **109**, 050506 (2012).
- [15] D. Sank, Z. Chen, M. Khezri, J. Kelly, R. Barends, B. Campbell, Y. Chen, B. Chiaro, A. Dunsworth, A. Fowler, E. Jeffrey, E. Lucero, A. Megrant, J. Mutus, M. Neeley, C. Neill, P. J. J. O'Malley, C. Quin-

- tana, P. Roushan, A. Vainsencher, T. White, J. Wenner, A. N. Korotkov, and J. M. Martinis, Measurement-induced state transitions in a superconducting qubit: Beyond the rotating wave approximation, *Phys. Rev. Lett.* **117**, 190503 (2016).
- [16] R. Lescanne, L. Verney, Q. Ficheux, M. H. Devoret, B. Huard, M. Mirrahimi, and Z. Leghtas, Escape of a driven quantum Josephson circuit into unconfined states, *Phys. Rev. Appl.* **11**, 014030 (2019).
- [17] R. Shillito, A. Petrescu, J. Cohen, J. Beall, M. Hauru, M. Ganahl, A. G. Lewis, G. Vidal, and A. Blais, Dynamics of transmon ionization, *Phys. Rev. Appl.* **18**, 034031 (2022).
- [18] J. Cohen, A. Petrescu, R. Shillito, and A. Blais, Reminiscence of classical chaos in driven transmons, *PRX Quantum* **4**, 020312 (2023).
- [19] M. Khezri, A. Opremcak, Z. Chen, K. C. Miao, M. McEwen, A. Bengtsson, T. White, O. Naaman, D. Sank, A. N. Korotkov, Y. Chen, and V. Smelyanskiy, Measurement-induced state transitions in a superconducting qubit: Within the rotating-wave approximation, *Phys. Rev. Appl.* **20**, 054008 (2023).
- [20] S. Hazra, W. Dai, T. Connolly, P. D. Kurilovich, Z. Wang, L. Frunzio, and M. H. Devoret, [Benchmarking the readout of a superconducting qubit for repeated measurements](#) (2024), [arXiv:2407.10934 \[quant-ph\]](#).
- [21] M. F. Dumas, B. Groleau-Paré, A. McDonald, M. H. Muñoz Arias, C. Lledó, B. D’Anjou, and A. Blais, Measurement-induced transmon ionization, *Phys. Rev. X* **14**, 041023 (2024).
- [22] B. M. Varbanov, F. Battistel, B. M. Tarasinski, *et al.*, Leakage detection for a transmon-based surface code, *npj Quantum Information* **6**, 102 (2020).
- [23] K. C. Miao, M. McEwen, J. Atalaya, *et al.*, Overcoming leakage in quantum error correction, *Nature Physics* **19**, 1780 (2023).
- [24] M. McEwen, D. Kafri, Z. Chen, *et al.*, Removing leakage-induced correlated errors in superconducting quantum error correction, *Nature Communications* **12**, 1761 (2021).
- [25] F. Battistel, B. Varbanov, and B. Terhal, Hardware-efficient leakage-reduction scheme for quantum error correction with superconducting transmon qubits, *PRX Quantum* **2**, 030314 (2021).
- [26] J. F. Marques, H. Ali, B. M. Varbanov, M. Finkel, H. M. Veen, S. L. M. van der Meer, S. Valles-Sanclemente, N. Muthusubramanian, M. Beekman, N. Haider, B. M. Terhal, and L. DiCarlo, All-microwave leakage reduction units for quantum error correction with superconducting transmon qubits, *Phys. Rev. Lett.* **130**, 250602 (2023).
- [27] N. Lacroix, L. Hofele, A. Remm, O. Benhayoune-Khadraoui, A. McDonald, R. Shillito, S. Lazar, C. Hellings, F. Swiadek, D. Colao-Zanuz, A. Flasby, M. B. Panah, M. Kerschbaum, G. J. Norris, A. Blais, A. Wallraff, and S. Krinner, [Fast flux-activated leakage reduction for superconducting quantum circuits](#) (2023), [arXiv:2309.07060 \[quant-ph\]](#).
- [28] M. D. Reed, B. R. Johnson, A. A. Houck, L. DiCarlo, J. M. Chow, D. I. Schuster, L. Frunzio, and R. J. Schoelkopf, Fast reset and suppressing spontaneous emission of a superconducting qubit, *Applied Physics Letters* **96**, 203110 (2010).
- [29] E. Jeffrey, D. Sank, J. Y. Mutus, T. C. White, J. Kelly, R. Barends, Y. Chen, Z. Chen, B. Chiaro, A. Dunsworth, A. Megrant, P. J. J. O’Malley, C. Neill, P. Roushan, A. Vainsencher, J. Wenner, A. N. Cleland, and J. M. Martinis, Fast accurate state measurement with superconducting qubits, *Phys. Rev. Lett.* **112**, 190504 (2014).
- [30] J. M. Gambetta, A. A. Houck, and A. Blais, Superconducting qubit with Purcell protection and tunable coupling, *Phys. Rev. Lett.* **106**, 030502 (2011).
- [31] I. Diniz, E. Dumur, O. Buisson, and A. Auffèves, Ultrafast quantum nondemolition measurements based on a diamond-shaped artificial atom, *Phys. Rev. A* **87**, 033837 (2013).
- [32] N. Didier, J. Bourassa, and A. Blais, Fast quantum nondemolition readout by parametric modulation of longitudinal qubit-oscillator interaction, *Phys. Rev. Lett.* **115**, 203601 (2015).
- [33] R. Dassonneville, T. Ramos, V. Milchakov, L. Planat, E. Dumur, F. Foroughi, J. Puertas, S. Leger, K. Bharadwaj, J. Delaforce, C. Naud, W. Hasch-Guichard, J. J. García-Ripoll, N. Roch, and O. Buisson, Fast high-fidelity quantum nondemolition qubit readout via a nonperturbative cross-kerr coupling, *Phys. Rev. X* **10**, 011045 (2020).
- [34] F. Pfeiffer, M. Werninghaus, C. Schweizer, N. Bruckmoser, L. Koch, N. J. Glaser, G. B. P. Huber, D. Bunch, F. X. Haslbeck, M. Knudsen, G. Krylov, K. Liegener, A. Marx, L. Richard, J. H. Romeiro, F. A. Roy, J. Schirck, C. Schneider, M. Singh, L. Södergren, I. Tsitsilin, F. Wallner, C. A. Riofrío, and S. Filipp, Efficient decoupling of a nonlinear qubit mode from its environment, *Phys. Rev. X* **14**, 041007 (2024).
- [35] Y. Ye, K. Peng, M. Naghiloo, G. Cunningham, and K. P. O’Brien, Engineering purely nonlinear coupling between superconducting qubits using a qurton, *Phys. Rev. Lett.* **127**, 050502 (2021).
- [36] Y. Ye, J. B. Kline, S. Chen, A. Yen, and K. P. O’Brien, Ultrafast superconducting qubit readout with the qurton coupler, *Science Advances* **10**, ead9094 (2024), <https://www.science.org/doi/pdf/10.1126/sciadv.ado9094>.
- [37] M. Malekakhlagh, W. Shanks, and H. Paik, Optimization of the resonator-induced phase gate for superconducting qubits, *Phys. Rev. A* **105**, 022607 (2022).
- [38] A. A. Chapple, A. McDonald, M. H. Muñoz-Arias, and A. Blais, [Robustness of longitudinal transmon readout to ionization](#) (2024), [arXiv:2412.07734 \[quant-ph\]](#).
- [39] See Supplemental Material for more information.
- [40] T. Connolly, Transmon readout in the large detuning limit – PART 1 : Design of the experiment, Presented at APS March Meeting, Session G47 , Minneapolis, MN, March 2024 (2024), abstract ID: G47.00005.
- [41] P. Kurilovich, Transmon readout in the large detuning limit – PART 2 : Results and their interpretation, Presented at APS March Meeting, Session G47 , Minneapolis, MN, March 2024 (2024), abstract ID: G47.00006.
- [42] V. Sivak, N. Frattini, V. Joshi, A. Lingenfelter, S. Shankar, and M. Devoret, Kerr-free three-wave mixing in superconducting quantum circuits, *Phys. Rev. Appl.* **11**, 054060 (2019).
- [43] S. Boutin, D. M. Toyli, A. V. Venkatramani, A. W. Edkins, I. Siddiqi, and A. Blais, Effect of higher-order nonlinearities on amplification and squeezing in Josephson parametric amplifiers, *Phys. Rev. Appl.* **8**, 054030 (2017).
- [44] C. C. Bultink, B. Tarasinski, N. Haandbæk, S. Poletto, N. Haider, D. J. Michalak, A. Bruno, and L. DiCarlo, General method for extracting the quantum efficiency of

- dispersive qubit readout in circuit QED, *Applied Physics Letters* **112**, 092601 (2018).
- [45] J. Gambetta, W. A. Braff, A. Wallraff, S. M. Girvin, and R. J. Schoelkopf, Protocols for optimal readout of qubits using a continuous quantum nondemolition measurement, *Phys. Rev. A* **76**, 012325 (2007).
- [46] B. D’Anjou and W. A. Coish, Optimal post-processing for a generic single-shot qubit readout, *Phys. Rev. A* **89**, 012313 (2014).
- [47] X. Xiao, J. Venkatraman, R. G. Cortiñas, S. Chowdhury, and M. H. Devoret, [A diagrammatic method to compute the effective hamiltonian of driven nonlinear oscillators](#) (2023), [arXiv:2304.13656 \[quant-ph\]](#).
- [48] M. F. Dumas, B. Groleau-Paré, A. McDonald, M. H. Muñoz-Arias, C. Lledó, B. D’Anjou, and A. Blais, Unified picture of measurement-induced ionization in the transmon (2024), [arXiv:2402.06615 \[quant-ph\]](#).
- [49] H. M. Wiseman and G. J. Milburn, Quantum theory of field-quadrature measurements, *Phys. Rev. A* **47**, 642 (1993).
- [50] J. Gambetta, W. A. Braff, A. Wallraff, S. M. Girvin, and R. J. Schoelkopf, Protocols for optimal readout of qubits using a continuous quantum nondemolition measurement, *Phys. Rev. A* **76**, 012325 (2007).
- [51] C. Wang, F.-M. Liu, H. Chen, Y.-F. Du, C. Ying, J.-W. Wang, Y.-H. Huo, C.-Z. Peng, X. Zhu, M.-C. Chen, C.-Y. Lu, and J.-W. Pan, [99.9%-fidelity in measuring a superconducting qubit](#) (2024), [arXiv:2412.13849 \[quant-ph\]](#).
- [52] H. P. Breuer and F. Petruccione, *The theory of open quantum systems* (Oxford University Press, Great Clarendon Street, 2002).
- [53] M. Boissonneault, J. M. Gambetta, and A. Blais, Non-linear dispersive regime of cavity qed: The dressed dephasing model, *Phys. Rev. A* **77**, 060305 (2008).
- [54] L. Labarca, O. Benhayoune-Khadraoui, A. Blais, and A. Parra-Rodriguez, Toolbox for nonreciprocal dispersive models in circuit quantum electrodynamics, *Phys. Rev. Appl.* **22**, 034038 (2024).
- [55] D. Sank, M. Khezri, S. Isakov, and J. Atalaya, [Balanced coupling in electromagnetic circuits](#) (2024), [arXiv:2406.08049 \[quant-ph\]](#).
- [56] J. Gambetta, A. Blais, M. Boissonneault, A. A. Houck, D. I. Schuster, and S. M. Girvin, Quantum trajectory approach to circuit qed: Quantum jumps and the zeno effect, *Phys. Rev. A* **77**, 012112 (2008).
- [57] J. Gambetta, A. Blais, D. I. Schuster, A. Wallraff, L. Frunzio, J. Majer, M. H. Devoret, S. M. Girvin, and R. J. Schoelkopf, Qubit-photon interactions in a cavity: Measurement-induced dephasing and number splitting, *Phys. Rev. A* **74**, 042318 (2006).
- [58] D. I. Schuster, A. Wallraff, A. Blais, L. Frunzio, R.-S. Huang, J. Majer, S. M. Girvin, and R. J. Schoelkopf, ac stark shift and dephasing of a superconducting qubit strongly coupled to a cavity field, *Phys. Rev. Lett.* **94**, 123602 (2005).
- [59] M. Boissonneault, J. M. Gambetta, and A. Blais, Improved superconducting qubit readout by qubit-induced nonlinearities, *Phys. Rev. Lett.* **105**, 100504 (2010).
- [60] M. Boissonneault, J. M. Gambetta, and A. Blais, Dispersive regime of circuit qed: Photon-dependent qubit dephasing and relaxation rates, *Phys. Rev. A* **79**, 013819 (2009).
- [61] J. Johansson, P. Nation, and F. Nori, Qutip: An open-source python framework for the dynamics of open quantum systems, *Computer Physics Communications* **183**, 1760 (2012).
- [62] J. Johansson, P. Nation, and F. Nori, Qutip 2: A python framework for the dynamics of open quantum systems, *Computer Physics Communications* **184**, 1234 (2013).
- [63] R. Gautier, Élie Genois, and A. Blais, Optimal control in large open quantum systems: the case of transmon readout and reset (2024), [arXiv:2403.14765 \[quant-ph\]](#).
- [64] P. Guilmin, R. Gautier, A. Bocquet, É. Genois, and D. Weiss, Dynamiqs: an open-source python library for gpu-accelerated and differentiable simulation of quantum systems (2024).
- [65] R. T. Lange, evosax: Jax-based evolution strategies, [arXiv preprint arXiv:2212.04180](#) (2022).

Supplemental Material for “Balanced cross-Kerr coupling for superconducting qubit readout”

Alex A. Chapple,^{1,*} Othmane Benhayoune-Khadraoui,^{1,*} Simon Richer,¹ and Alexandre Blais^{1,2}

¹*Institut Quantique and Département de Physique,
Université de Sherbrooke, Sherbrooke J1K 2R1 Quebec, Canada*
²*Canadian Institute for Advanced Research, Toronto, ON, Canada*

S1. BASICS OF BRANCH ANALYSIS

In this section, we outline the basic theory behind branch analysis, a numerical tool that can help predict the critical photon number for the onset of ionization. For a more detailed discussion of this approach, see Ref. [17, 21].

To simplify the discussion in this section, we consider the transmon qubit, however, the method also works for other types of qubits. We begin with the undriven, coupled transmon (tr) and resonator (r) Hamiltonian generically given by

$$\hat{H} = \hat{H}_{\text{tr}} + \hat{H}_{\text{r}} + \hat{H}_{\text{int}}. \quad (\text{S1})$$

Diagonalizing the above Hamiltonian results in a set of eigenvectors $\{|\lambda\rangle\}$. For each considered level j_t of the transmon, we find the eigenvector from $\{|\lambda\rangle\}$ that maximizes the overlap $|\langle j_t, 0_r | \lambda \rangle|^2$ and label this eigenvector as $|\overline{j_t, 0_r}\rangle$, the overline denoting a dressed state. We then use these states $|\overline{j_t, 0_r}\rangle$ to recursively assign a label to all remaining states: $|\overline{j_t, n_r + 1}\rangle$ is defined as the unassigned eigenstate $|\lambda\rangle$ which maximizes the overlap $|\langle \lambda | \hat{a}^\dagger | \overline{j_t, n_r} \rangle|^2$. Repeating this for each transmon index j_t results in a set of dressed states $B_{j_t} = \{|\overline{j_t, n_r}\rangle\}$ which we refer to as branches.

Using these branches, we can compute the average transmon and resonator populations. An ionization process can be identified when the branches for the ground or excited state swaps with a branch of a higher excited state. The photon number at which this occurs is reported as the critical photon number.

S2. EXTRACTING PURCELL DECAY

In this section, we discuss how the Purcell-limited lifetimes T_1^{Purcell} shown in Fig. 1(c) are extracted. For each value of the charge-charge coupling J , we simulate a T_1 experiment by initializing the qubit in its dressed excited state $|\overline{1_t, 0_r}\rangle$ and evolving it according to

$$\frac{d\hat{\rho}}{dt} = -i[\hat{H}, \hat{\rho}] + \kappa \mathcal{D}[\hat{a}'] \hat{\rho}, \quad (\text{S2})$$

where \hat{H} is given by Eq. (1). The transmon parameters are set to $E_c/2\pi = 300$ MHz, $E_{J,\text{total}}/E_C = 50$, and the resonator parameters to $\omega_r/2\pi = 9.375$ GHz, $Z_r = 25 \Omega$,

and $\kappa/2\pi \simeq 2\chi_z/2\pi = 8$ MHz. The coupling Josephson junction is characterized by $E_{J_c}/2\pi = 4$ GHz.

In the above expression, the collapse operator \hat{a}' is expressed in the dressed basis as [52]

$$\hat{a}' = \sum_{\substack{\lambda', \lambda \\ E_{\lambda'} \geq E_\lambda}} \langle \lambda | \hat{a} | \lambda' \rangle | \lambda \rangle \langle \lambda' |, \quad (\text{S3})$$

where $\{|\lambda\rangle\}$ are the eigenstates of the transmon-resonator Hamiltonian \hat{H} as defined above. Here, we consider only energy-loss processes, assuming the bath is in its vacuum state. To extract T_1^{Purcell} , we fit the excited-state population $|\overline{1_t, 0_r}\rangle \langle \overline{1_t, 0_r}|$ to a single exponential decay, $e^{-t/T_1^{\text{Purcell}}}$.

The Purcell decay obtained from this method assumes a flat bath spectrum, i.e., $\kappa(\omega) = \kappa(\omega_r) \equiv \kappa$. In practice, however, the qubit probes the bath at its own frequency, which for these parameters is $\bar{\omega}_q/2\pi = 5.672$ GHz, rather than the resonator frequency. Therefore, to achieve a more accurate estimate, we normalize the T_1^{Purcell} value obtained above by a factor of $\kappa/\kappa(\bar{\omega}_q)$ [8, 53, 54], which is approximately $(\bar{\omega}_r/\bar{\omega}_q)^2 \simeq 2.75$, assuming that all photon losses originate from coupling to the readout feedline [8, 54].

S3. TRANSMON IONIZATION WITH JUNCTION READOUT

In this section, we outline how the cancellation condition in junction readout suppresses measurement-induced transitions out of the computational subspace, and discuss physically meaningful metrics for relating critical photon numbers to readout performance.

A. Effect of cancellation condition on ionization

As stated in the main text, the matrix element eliminated by the cancellation condition Eq. (3) is also precisely the matrix element responsible for transitioning the ground state of the transmon to the first excited state when measurement-induced transitions to higher excited states occur. Additionally, the matrix element that connects the first excited state to the second excited state is also approximately suppressed when the condition Eq. (3) is satisfied. Therefore, by eliminating these

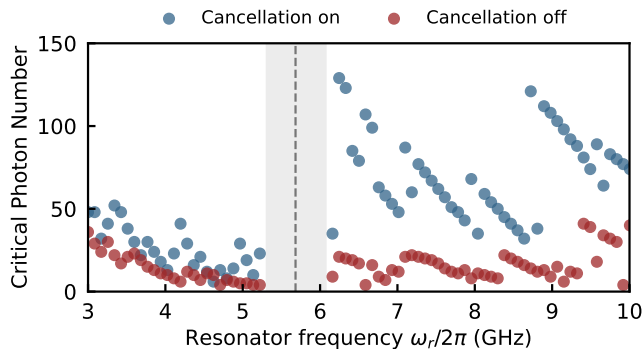


FIG. S1. Critical photon numbers for varying resonator frequencies ω_r . The red dots indicate when there is no coupling capacitance, and the blue dots are for where the cancellation condition is met. Here the transmon parameters are the same as in Fig. 4 and the resonator impedance is $Z_r = 35 \Omega$. The coupling junction energy is $E_{Jc}/2\pi = 7.8$ GHz, resulting in $\chi_z/2\pi \simeq 9$ MHz when the cancellation condition is met.

matrix elements the likelihood of multiphoton processes causing the transmon to jump in excitation is expected to be reduced.

Fig. S1 shows the critical photon numbers for varying resonator frequencies, both for when the cancellation condition Eq. (3) is satisfied or not. When the cancellation condition is met, we observe as expected that the critical photon numbers increase.

It is worth mentioning that for the dispersive readout, canceling the $0 \leftrightarrow 1$ matrix element responsible for Purcell decay would also result in canceling most of the charge-charge coupling-based dispersive shift that is essential for readout [39]. Alternatively, as recently discussed in Ref. [55] in the context of dispersive readout, one could cancel parasitic matrix elements involving higher-energy states that are causing ionization without compromising the dispersive shift. However, no parameter set can cancel *all* parasitic matrix elements simultaneously. Furthermore, since these cancellations involve higher-energy states, they are sensitive to fluctuations in the gate charge. Consequently, this balanced coupling strategy does not push ionization to larger photon numbers for dispersive readout.

B. Critical photon number threshold

In Fig. 3, we set the critical photon number threshold to be $n_{\text{crit}} = 35$. In this section, we show that the parameters chosen correspond to a physically meaningful readout performance metric. We begin with the analytical expression for the signal-to-noise ratio (SNR) in the long-time limit [56]

$$\text{SNR} \simeq \frac{2\epsilon}{\kappa} \sqrt{4\eta\kappa t_m}. \quad (\text{S4})$$

In the above expression, ϵ is the drive amplitude, κ is the resonator decay rate, η is the measurement efficiency, and t_m is the measurement time. Assuming that the resonator is driven at its Lamb-shifted frequency, and for the optimal ratio $\kappa \simeq 2\chi$, which we ensure to be approximately satisfied in our numerical simulations, we can relate the above expression of SNR to the average photon number in the resonator \bar{n} as

$$\text{SNR} \simeq 2\sqrt{2\eta\bar{n}\kappa t_m}, \quad (\text{S5})$$

which simplifies to $\text{SNR} \simeq 2\sqrt{2\eta\bar{n}}$ for a measurement time of order $t_m \sim 1/\kappa$, corresponding to the resonator reaching its steady-state.

Choosing the threshold to be $n_{\text{crit}} = 35$, we must ensure that the maximum number of photons placed in the resonator remains well below this threshold to minimize leakage. Given the approximately coherent-state nature of the resonator field during readout, as discussed in the main text, we model the photon number distribution as Poissonian and require its tail to have minimal overlap with the critical photon number. For instance, a safe metric is to limit this overlap to be approximately 0.01%. This condition translates to an average photon number \bar{n} satisfying $n_{\text{crit}} = \bar{n} + 4\sqrt{\bar{n}}$, which yields $\bar{n} \simeq 18$.

For a measurement efficiency of $\eta = 0.5$, in line with state-of-the-art experiments [10, 13, 20], we find $\text{SNR} \simeq 6$. The SNR can be linked to the measurement to the readout fidelity F as [56]

$$F = 1 - \frac{1}{2} \text{erfc} \left(\frac{\text{SNR}}{2\sqrt{2}} \right). \quad (\text{S6})$$

Note that this definition implies that $F \in [0.5, 1]$. For $\text{SNR} \simeq 6$, we find $F \simeq 0.9999(8)$, suggesting that the above choice of parameters and threshold comfortably lead to a readout fidelity exceeding 99.99%. Of course, the above expression does not account for distortions to the coherent states, transient dynamics of the readout, the T_1 limit of the transmon, and other effects. Nevertheless, they provide a useful and simple metric for relating readout performance to the critical photon number. In the main text and Sec. S5 we go beyond these simple approximations.

S4. PHOTON NUMBER DEPENDENT DISPERSIVE SHIFT

The dispersive shift is often defined as $\chi_z = (E_{1,1} - E_{1,0} - E_{0,1} + E_{0,0})/2$, where E_{i_t, n_r} denotes the energy of the dressed state $|i_t, n_r\rangle$ of the transmon-resonator system, as labeled in Sec. S1. However, this definition of the dispersive shift is based on the low-energy spectrum of the transmon-resonator system and becomes inaccurate even for moderate photon numbers in the resonator [57, 58].

In Fig. S2(a), we compare the magnitude of the dispersive shift at different resonator photon numbers, defined

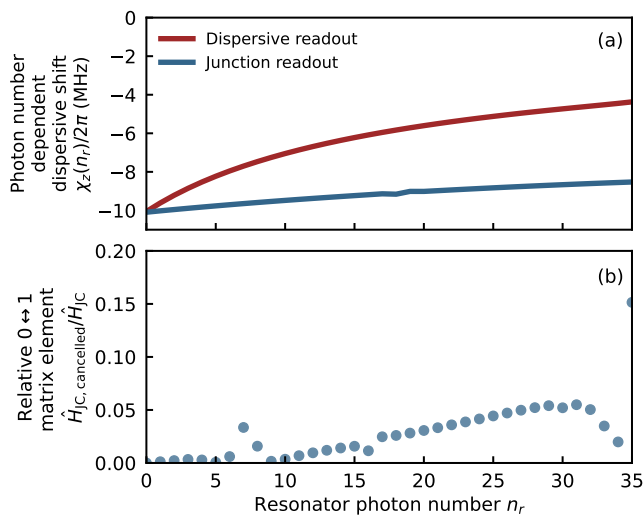


FIG. S2. (a) Photon number dependent dispersive shift χ_z for varying resonator photon numbers n_r . For both readout methods, we choose parameters such that $\chi_z(0)/2\pi \simeq 10$ MHz. For junction readout, the transmon parameters are the same as in Fig. 4. For dispersive readout, the transmon parameters are the same as in Fig. 3, but the resonator frequency was set to $\omega_r/2\pi = 6.246$ GHz, with a coupling strength of $g/2\pi = 114$ MHz, to ensure a high critical photon number as shown in Fig. 3. (b) The ratio between the $0 \leftrightarrow 1$ matrix element of the Jaynes-Cummings interaction Hamiltonian with optimal charge-charge coupling $\hat{H}_{JC,cancelled}$ to that without charge-charge coupling \hat{H}_{JC} , at varying resonator photon numbers, See Sec. S4 for further details.

as

$$\chi_z(n_r) = (E_{1_t, n_r+1} - E_{1_t, n_r} - E_{0_t, n_r+1} + E_{0_t, n_r})/2, \quad (S7)$$

for both dispersive readout and junction readout. At zero photons in the resonator, the parameters are taken such that the dispersive shift is $\chi_z/2\pi \simeq 10$ MHz for both readout methods. For dispersive readout, we find that at high photon numbers the magnitude of the dispersive shift is reduced by more than a half. Conversely, for junction readout the magnitude of the dispersive shift remains approximately constant. For example, at $n_r = 35$, the dispersive shift is reduced to $\chi_z(n_r = 35)/2\pi = -4.37$ MHz for dispersive readout, while $\chi_z(n_r = 35)/2\pi = -8.526$ MHz for junction readout.

We attribute the significant difference between dispersive readout and junction readout to the nature of the coupling interaction. In the dispersive case, exact diagonalization of the Jaynes-Cummings Hamiltonian reveals that, beyond the linear dispersive regime, higher-order contributions to $\chi_z(n_r)$ scales as $\sim (g/\Delta)^{2n_r}$ [53, 59, 60]. Conversely, for the $\cos \hat{\varphi}_r \cos \hat{\varphi}_t$ interaction, these higher-order contributions scale as $\varphi_{z\text{pfr}}^{2n_r}$ [38]. For the chosen set of parameters optimized to ensure high n_{crit} and χ_z for both readout methods, we find $\varphi_{z\text{pfr}} < |g/\Delta|$, and while

g/Δ cannot be made arbitrarily small—otherwise, the leading-order dispersive shift becomes negligible— $\varphi_{z\text{pfr}}$ can be reduced by decreasing the resonator impedance, without sacrificing the leading-order dispersive shift.

Thus, even when both junction readout and dispersive readout are designed with the same initial dispersive shift $\chi_z(0)$, and both schemes are optimized for high critical photon numbers, junction readout is expected to enable faster measurement, particularly at higher photon numbers.

In addition, Fig. S2(b) shows the ratio between the matrix elements $|\langle 0_t, n_r + 1 | \hat{H}_{JC,cancelled} | 1_t, n_r \rangle|$ and $|\langle 0_t, n_r + 1 | \hat{H}_{JC} | 1_t, n_r \rangle|$ for varying resonator photon numbers. Here, $\hat{H}_{JC,cancelled} = -E_{JC} \sin \hat{\varphi}_t \sin \hat{\varphi}_r + J \hat{n}_t \hat{n}_r$ with J chosen to satisfy Eq. (3), and $\hat{H}_{JC} = -E_{JC} \sin \hat{\varphi}_t \sin \hat{\varphi}_r$. We note that even at large resonator photon numbers, the ratio of the matrix elements remains small, showing that the cancellation condition remains effective during readout when the resonator is populated.

S5. DETAILS ON READOUT SIMULATIONS

In this section, we outline the details of our single-shot readout simulations. For the heterodyne readout simulations of Fig. 4, we use QuTiP’s solver [61, 62] to integrate the stochastic Schrödinger equation [49]

$$\begin{aligned} d\psi(t) = & -i\hat{H}\psi(t)dt \\ & - \left(\frac{\kappa}{2} \hat{a}^\dagger \hat{a} - \frac{\kappa}{4} [\langle \hat{x} \rangle + i\langle \hat{p} \rangle] \hat{a} + \frac{\kappa}{16} [\langle \hat{x} \rangle^2 + \langle \hat{p} \rangle^2] \right) \psi(t) \\ & + \sqrt{\frac{\kappa}{2}} \left(\hat{a} - \frac{\langle \hat{x} \rangle}{2} \right) \psi(t) dW_x \\ & - \sqrt{\frac{\kappa}{2}} \left(i\hat{a} + \frac{\langle \hat{p} \rangle}{2} \right) \psi(t) dW_p. \end{aligned} \quad (S8)$$

Here, \hat{H} is the sum of Eq. (1) and the drive term $\hat{H}_d = -i\epsilon(t)(\hat{a} - \hat{a}^\dagger)$, where $\epsilon(t)$ is the resonator drive amplitude, with its explicit time dependence provided below. Additionally, κ is the resonator decay rate, and $\hat{x} = \hat{a} + \hat{a}^\dagger$, and $\hat{p} = i(\hat{a}^\dagger - \hat{a})$ are the measured quadratures. In the above expression, the first and second lines describe the deterministic evolution of the state $\psi(t)$ while the last two terms describe the measurement back action. The two dW_i are independent stochastic Wiener increments satisfying $\mathbb{E}[dW_i] = 0$ and $\mathbb{E}[dW_i^2] = dt$. Both quadratures, x and p , have their own independent Wiener increments, denoted by their respective subscripts.

For each simulated trajectory, we demodulate the signal with $e^{i\omega_d t}$ where ω_d is the drive frequency. The demodulated signal for the x and p quadratures are then integrated with the real and imaginary part of the optimal weight function $\langle a_e(t) \rangle - \langle a_g(t) \rangle$, respectively. The results are shown in Fig. 4(a) and (b). At each integration time we find the optimal discriminator in the IQ-plane which gives us the minimum assignment error defined as $\varepsilon = (P(e|g) + P(g|e))/2$, which is then shown in Fig. 4(c).

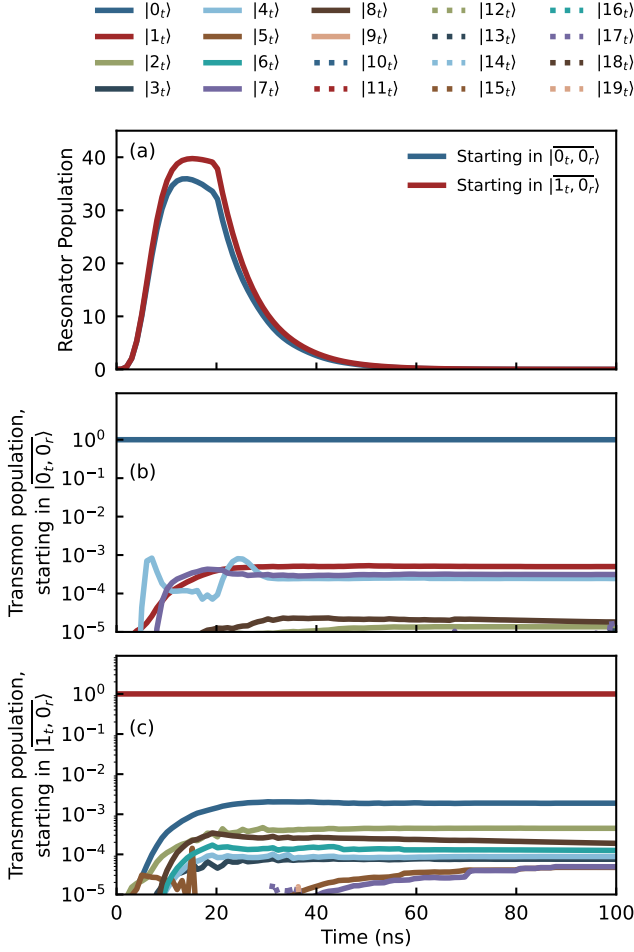


FIG. S3. (a) Resonator population as a function of integration time, for when the transmon is prepared in the ground or excited state. (b) and (c) show the population of the first 20 energy levels of the transmon during the readout simulation, when starting in the ground and excited state, respectively. The circuit parameters are as given in Fig. 4.

We found that using $nsubsteps = 12,000$, with the transmon dimension set to 7 and resonator dimension set to 75 showed good convergence.

As mentioned in the main text, we use a two-step pulse in order to fill the resonator with a large number of photons rapidly. The pulse shape is given as in Ref. [38],

$$\epsilon(t) = \frac{4t\sqrt{\bar{n}}}{\tau^2} e^{-(t/\tau)^2} + \kappa\sqrt{\bar{n}}(1 - e^{-(t/\tau)^2}), \quad (\text{S9})$$

where τ and κ determine the speed at which the resonator gets populated. Here, we set τ to be 6 ns. As we show in Sec. S7, optimizing the pulse shape with quantum optimal control techniques results in further improvements in performance.

The results from the heterodyne readout simulations are compared to coherent state approximated assignment errors. Assuming the states in the resonator to be coherent states, we can get an expression for the optimal

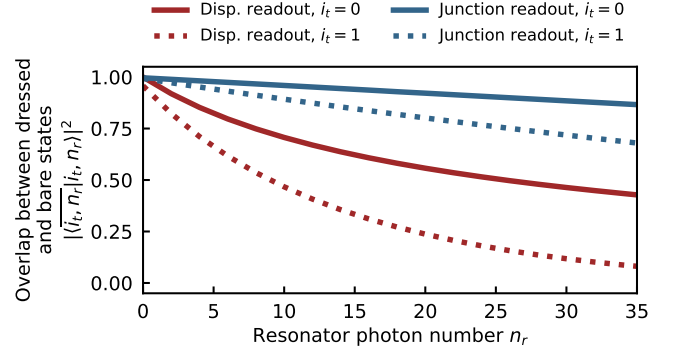


FIG. S4. Overlap between the dressed states $|\bar{i}_t, \bar{n}_r\rangle$ and bare states $|i_t, n_r\rangle = |i_t\rangle \otimes |n_r\rangle$ at varying resonator photon numbers, for both junction readout and dispersive readout. The parameters for both readout methods are the same as was described in Fig. S2.

signal-to-noise ratio (SNR) as [44]

$$\text{SNR}(t_m) = \sqrt{2\kappa\eta \int_0^{t_m} |\alpha_e(t) - \alpha_g(t)|^2 dt}, \quad (\text{S10})$$

where η is the measurement efficiency, κ is the resonator decay rate, t_m is the integration time, and $\alpha_{e/g}(t)$ is the resonator field. Using the above formula for the optimal SNR, we can compute the assignment error as [12, 45]

$$\epsilon(t_m) = \frac{1}{2} \text{erfc} \left(\frac{\text{SNR}(t_m)}{2\sqrt{2}} \right) + \frac{t_m}{2T_1}, \quad (\text{S11})$$

where erfc is the complementary error function and T_1 is the transmon lifetime. The coherent state approximated assignment errors are computed from performing Monte-Carlo simulations using QuTiP's *mcsolve* solver [61, 62] to get the resonator's field $\alpha_{e/g}(t)$. The Hamiltonian and the parameters used for the simulations are the same as what was used for the heterodyne readout simulations. The collapse operator is $\sqrt{\kappa}\hat{a}$ and we use 512 trajectories for the Monte-Carlo simulations.

S6. LEAKAGE AND QNDNESS

In this section, we characterize the leakage rates in our junction readout simulations and provide general comparisons of the expected leakage rates between dispersive and junction readout. Fig. S3(a) shows the resonator population as a function of integration time for the junction readout simulation parameters used in Fig. 4, obtained from the Monte-Carlo readout simulation described in Sec. S5 by preparing the qubit in the ground state (blue) or excited state (red).

As previously mentioned, we employ a two-step pulse, stopping the drive at $t = 20$ ns, letting the resonator to decay rapidly thereafter with a rate $\kappa/2\pi = 2\chi_z/2\pi \simeq 20$

Description	Analytical formula	Weight	Hyperparameters
Inverse signal-to-noise ratio	$\left(2\eta\kappa \int_0^{t_m} \alpha_e(t) - \alpha_g(t) ^2 dt\right)^{-1/2}$	1.0	$\kappa/2\pi \simeq 20$ MHz
Maximum pulse amplitude	$\frac{1}{t_m} \int_0^{t_m} \text{ReLU}(\epsilon(t) - \epsilon_{\max}) dt$	10^{-4}	$\epsilon_{\max}/2\pi = 700$ MHz
Maximum resonator population	$\sum_{i=g,e} \frac{1}{t_m} \int_0^{t_m} \text{ReLU}(\text{Tr}[\hat{a}^\dagger \hat{\rho}_i(t)] - \bar{n}_{\max}) dt$	10^{-3}	$\bar{n}_{\max} = 40$
Pulse smoothness	$\frac{1}{t_m} \int_0^{t_m} (\partial\epsilon(t)/\partial t) dt$	10^{-3}	–

TABLE S1. Summary of readout cost function used for optimizing the pulse, alongside their analytical expressions, relative weights, and the parameters used. ReLU denotes the rectified linear unit defined as $\text{ReLU}(x) = 0$ for $x \leq 0$ and $\text{ReLU}(x) = x$ for $x > 0$.

MHz. To quantify the QNDness, we track the population of each transmon level i_t by calculating $P_{i_t}(t) = \text{Tr}[\sum_{n_r} |i_t, n_r\rangle\langle i_t, n_r| \hat{\rho}(t)]$. The transmon populations as a function of time for initial states $|0_t, 0_r\rangle$ and $|1_t, 0_r\rangle$ are shown in Fig. S3(b) and (c), respectively. From Fig. S3(a) we identify the time at which the resonator population drops below 10^{-2} and use this to evaluate the population of the ground and first excited states of the transmon to characterize the quantum nondemolition (QND) nature of the readout. For these parameters, the QND fidelity was found to be 99.89% when starting in the ground state and 99.71%, when starting in the first excited state.

While weak resonances in the transmon-resonator spectrum are often disregarded when analyzing measurement-induced transitions, they are crucial for characterizing leakage rates. The extent to which the transmon leaks depends significantly on the degree of hybridization between the transmon and resonator states [19, 21]. To fully quantify this hybridization, in Fig. S4, we plot the overlap between the bare and dressed states of the transmon-resonator system for various resonator photon numbers. We find that for dispersive readout, the overlap decreases rapidly even at moderate photon numbers, particularly when the system starts in the first excited state. In contrast, for junction readout, the overlap exhibits only minimal variation with increasing photon numbers, suggesting that junction readout results in less leakage compared to dispersive readout, as the system's state deviates less from its initial qubit state during the readout process.

S7. QUANTUM OPTIMAL CONTROL

In this section, we outline the quantum optimal control method used to enhance the readout fidelity and speed, as shown in Fig. 4(c). These simulations are based on Ref. [63] which makes use of the open source library dynamiqs [64]. We also use the evosax library [65] to efficiently explore the large optimization parameter space with the Covariance Matrix Adaptation (CMA) evolution strategy.

As discussed in Ref. [63], the readout pulse is divided into 1 ns time bins, representing the parameters to be optimized, and filtered through a Gaussian envelope with a 500 MHz bandwidth. Furthermore, the maximum amplitude is limited to $\epsilon_{\max}/2\pi = 700$ MHz whilst ensuring that the photon population does not exceed $\bar{n}_{\max} = 40$ to remain consistent with our previous simulations (see Fig. 4 and Sec. S5).

The cost function consists of a weighted sum of 4 components, as summarized in Table S1: the inverse of the signal-to-noise ratio (SNR), the maximum resonator population, the maximum amplitude and the pulse smoothness. The optimization is performed for integration times between 10 and 30 ns. Although the pulse shapes vary slightly with integration time, all optimized pulses resemble a two-step pulse and reach the maximum resonator population, see Fig. S5 (b) and (c). Crucially, as shown in Fig. S5 (a), the optimized pulses outperform the analytical pulse described in Sec. S5 at all integration times, reaching a readout fidelity of 99.99% in $t_m \simeq 18$ ns. Even when accounting for a finite T_1 of 120 μ s and a reduced measurement efficiency of $\eta = 0.5$, the optimal pulse achieves 99.99% readout fidelity in $t_m \simeq 28$ ns.

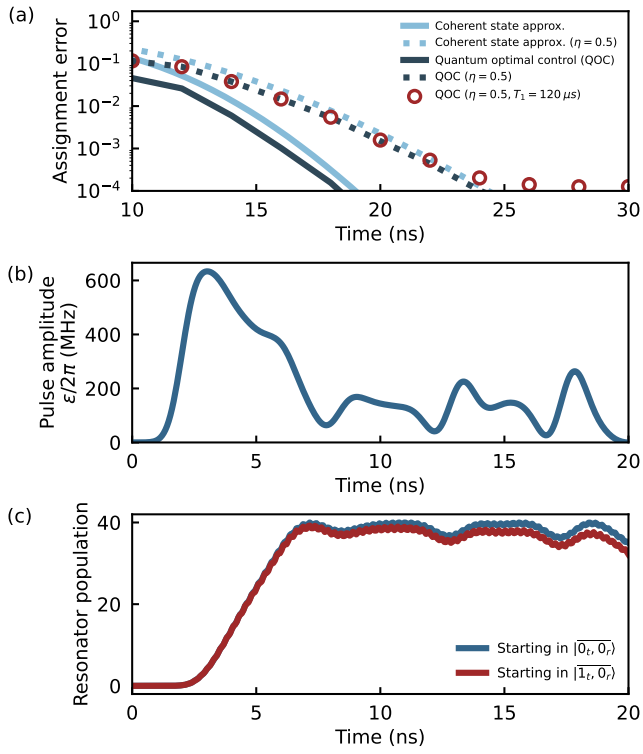


FIG. S5. (a) Assignment error obtained from the coherent state approximation (light blue, see Fig. 4(c)) and quantum optimal control (dark blue). Solid lines correspond to the ideal efficiency case of $\eta = 1$, while dashed lines correspond to reduced efficiency of $\eta = 0.5$, based on state-of-the-art values. Red circles indicate when both finite lifetime ($T_1 = 120 \mu s$) and reduced readout efficiency ($\eta = 0.5$) are taken into account. For both methods, the parameters are identical to those in Fig. 4. (b) Optimal pulse shape obtained for an integration time of $t_m = 20$ ns and (c) the corresponding resonator population.